Two-Dimensional Transport-Induced Linear Magneto-Resistance in Topological Insulator Bi_2Se_3 Nanoribbons

Hao Tang,[†] Dong Liang,[†] Richard L. J. Qiu, and Xuan P. A. Gao*

Department of Physics, Case Western Reserve University, Cleveland, Ohio 44106, United States. [†]These authors contributed equally to this work.

ABSTRACT We report the study of a novel linear magneto-resistance (MR) under perpendicular magnetic fields in Bi_2Se_3 nanoribbons. Through angular dependence magneto-transport experiments, we show that this linear MR is purely due to two-dimensional (2D) transport, in agreement with the recently discovered linear MR from 2D topological surface state in bulk Bi_2Te_3, and the linear MR of other gapless semiconductors and graphene. We further show that the linear MR of Bi_2Se_3 nanoribbons persists to room temperature, underscoring the potential of exploiting topological insulator nanomaterials for room-temperature magneto-electronic applications.

KEYWORDS: topological insulator · Bi_2Se_3 · nanoribbon · linear magneto-resistance · two-dimensional transport

Topological insulators (TIs) are quantum materials with a conducting gapless surface state on the surface or edge of an insulating bulk,[1−4] holding great promise in the fundamental study of topological ordering in condensed matter systems and applications in spintronic devices for a spin-polarized surface state. The spin polarization and suppressed backscattering render 2D topological surface states an attractive platform for high mobility charge- and spin-transport devices. Recently, Bi_2Se_3 and related materials have been proposed[5] and confirmed[6−8] as three-dimensional (3D) TIs with a single Dirac cone for the surface state. Among these materials, Bi_2Se_3, which is a pure compound rather than an alloy like Bi_xSb_{1-x},[9] has a larger bulk band gap (0.3 eV) and is thought to be promising for room-temperature applications. Although the existence of a topological surface state in Bi_2Se_3 has been established by surface-sensitive techniques such as angle-resolved photoemission spectroscopy,[6,7] extracting the transport properties of the 2D surface state in 3D TIs has been plagued by the more dominating conductivity from bulk carriers.[10−18] With extremely high surface-to-volume ratio and thus larger surface contribution in transport, nanostructures of TIs are useful to distinguish 2D surface transport from 3D bulk transport in the heated study of topological surface state. Indeed, Aharonov−Bohm (AB) oscillations were discovered in Bi_2Se_3 nanoribbons in the parallel magnetic field induced MR, proving the existence of a coherent surface conducting channel.[10] In this study, we explore the magneto-transport phenomena in Bi_2Se_3 nanoribbons in a magnetic field perpendicular to the surface of nanoribbons and uncover a novel linear MR effect that is sensitive only to the perpendicular component of the magnetic field (B) and absent in parallel field. This 2D magneto-transport-induced linear MR is weakly temperature dependent and survives at room temperature, suggesting the possibility of using 2D topological surface transport in room-temperature magneto-electronic applications.

RESULTS AND DISCUSSION

Pure Bi_2Se_3 nanoribbons are synthesized in a horizontal tube furnace *via* the vapor−liquid−solid mechanism with gold particles as catalysts, similar to that in the literature.[10,11] Typical Bi_2Se_3 nanoribbons have thickness ranging from 50 to 400 nm and widths ranging from 200 nm to several μms, as shown in the scanning electron microscope (SEM) image in Figure 1a. The transmission electron microscope (TEM) image demonstrates that nanoribbons have smooth side walls and flat surfaces, as shown in Figure 1b for a 200 nm wide nanoribbon. Energy-dispersive X-ray spectroscopy (EDX) analyses reveal uniform chemical composition with a Bi/Se atomic ratio about 2:3, indicating stoichiometric Bi_2Se_3. High-resolution TEM imaging and 2D Fourier transformed electron diffraction measurements in Figure 1c and d demonstrate that the samples are

* Address correspondence to xuan.gao@case.edu.

Received for review July 3, 2011 and accepted July 27, 2011.

Published online July 27, 2011
10.1021/nn2024607

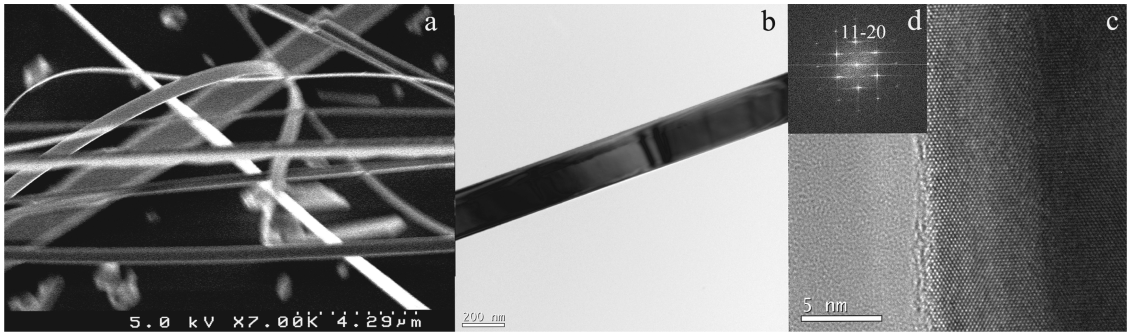

Figure 1. Morphology and crystal structure of Bi_2Se_3 nanoribbons. (a) SEM image of as-grown Bi_2Se_3 nanowires and ribbons. (b) TEM image showing the shape, flat surfaces, and edges of a ribbon with 200 nm width. (c) High-resolution TEM image of the edge of the Bi_2Se_3 nanoribbon showing the smooth surface. Scale bar is 5 nm. (d) The Fourier transform electron diffraction pattern indicates the single-crystalline quality of the nanoribbon. The growth direction of the nanoribbon is along [11$\bar{2}$0].

single-crystalline rhombohedral phase and grow along the [11$\bar{2}$0] direction. The upper and lower surfaces are the (0001) planes. The as-grown samples are suspended in ethanol by sonication and dispersed on a heavily doped Si substrate with 300 nm SiO_2 on its surface. Photolithography is used to pattern four electrodes contacting a single nanoribbon, as shown in the SEM picture in Figure 2a inset. The electrodes consist of 150 nm Pd with a 5 nm Ti adhesion layer formed *via* e-beam evaporation and lift-off. Ohmic contacts are obtained without annealing. The transport measurements are performed in a Quantum Design PPMS with the standard low-frequency lock-in technique. Four-terminal resistance of the nanoribbons is obtained by flowing a current I (typically 0.1−1 μA) through the two outer contacts and monitoring the voltage drop V between the two inner contacts (typical spacing ~2 μm) (Figure 2a inset).

The resistance R of nanoribbon sample #1 as a function of magnetic field B is shown in Figure 2a at temperature T = 2 K. This sample was mounted on a rotating stage such that its surface (a−b plane) could be tilted in the magnetic field by an arbitrary angle θ (Figure 2b inset). Using an atomic force microscope (AFM), we measured a sample width of 560 nm and thickness of 100 nm for this nanoribbon. In perpendicular magnetic field (θ = 0), the sample exhibited the largest magneto-resistance, which is positive and becomes very linear above a characteristic field of 1−2 T. This MR gradually decreased when the sample was tilted away from perpendicular configuration and eventually became almost negligible in the parallel magnetic field configuration (θ = 90°). It has been known for a long time that regular metals exhibit quadratic MR (*i.e.*, $\Delta R \propto B^2$) at low fields ($\omega_c\tau < 1$, with ω_c and τ being the cyclotron frequency and mean scattering time), and this MR would saturate at high field ($\omega_c\tau > 1$).[19−21] Therefore, observing a nonsaturating linear MR in strong magnetic field is interesting in both the fundamental magneto-transport phenomena

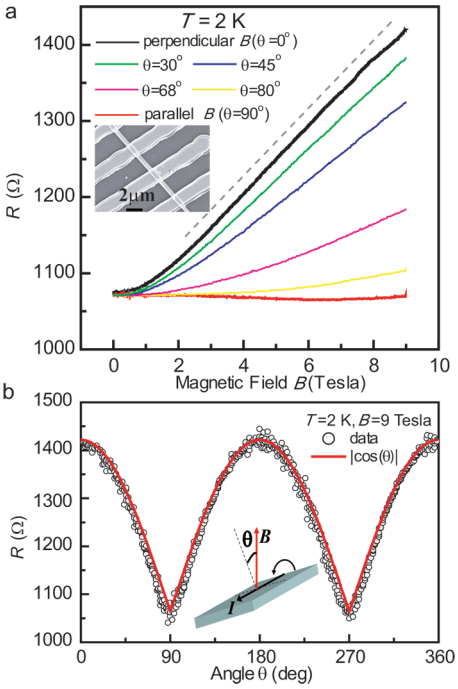

Figure 2. Two-dimensional magneto-transport-induced linear magneto-resistance (MR) in Bi_2Se_3 nanoribbons. (a) Resistance R *vs* magnetic field B of a Bi_2Se_3 nanoribbon (sample #1) at 2 K and different tilt angle between sample surface and the magnetic field. The gray dashed line highlights the linear MR above the 1 T perpendicular magnetic field. The inset shows an SEM image of a nanoribbon contacted by four leads in the four-probe transport measurement setup. (b) R *vs* the tilt angle θ in a fixed magnetic field of 9 T and at T = 2 K. The data are seen to follow the function $|\cos(\theta)|$ (solid red line). In both (a) and (b), the magnetic field is always perpendicular to the current when the sample is rotated with respect to B (inset).

and magnetic sensor applications.[19,22] Very recently, a linear MR was observed in low-doped Bi_2Te_3 crystal flakes that showed 2D surface-state transport.[18] It is thus encouraging that linear MR is now also observed in topological insulator Bi_2Se_3 nanoribbons directly grown from chemical synthesis, in which case the materials can be grown and assembled in large scale for scaled up nanoelectronics applications.[23] The

nature of this linear MR in Bi_2Se_3 nanoribbons is the focus of this paper.

In the electrical transport study of topological insulator Bi_2Se_3 or Bi_2Te_3, it is important to distinguish the 3D transport due to bulk carriers from the 2D surface-state transport since the Se or Te vacancies may induce high electron concentration and push the Fermi level into the bulk conduction band. One standard way to check if the magneto-transport is 2D or 3D is the angular dependence of the magneto-transport.[13,14,18] For 2D surface-state transport, the magneto-transport will respond only to the perpendicular component of the magnetic field $B\cos(\theta)$. In Figure 2b, we show the resistance of sample #1 as a function of rotation angle when the sample was rotated in a 9 T magnetic field at 2 K (inset). The measured $R(\theta)$ dependence is seen to have wide peaks around the perpendicular field configuration ($\theta = 0°$, 180°) and dips with cusp around the parallel field configuration ($\theta = 90°$, 270°). In fact, the experimental data have an excellent agreement with the functional form $|\cos(\theta)|$ (red line in Figure 2b). This suggests that the sample is responsive only to the perpendicular component of B at arbitrary tilt angle, and thus the linear MR is a 2D magneto-transport effect.

In the strongest perpendicular magnetic fields, $R(B)$ of sample #1 showed weak oscillations on top of the linear MR. These are Shubnikov–de Haas (SdH) oscillations due to the formation of quantized energy levels (Landau levels) of orbital motions of electrons. We analyze SdH oscillations in another sample (#2) in which these oscillations are more pronounced to extract the carrier density and further demonstrate the 2D nature of the Fermi surface. Sample #2 had a width of 300 nm and thickness of 25 nm as measured by AFM. Figure 3a shows the *R vs B* from zero to 9 T of sample #2 at various tilt angles. The sheet resistivity ρ is shown on the right side of the *y*-axis, after taking into account the ratio between the length and width of the nanoribbon. Similar to sample #1, in the perpendicular field, a linear MR was observed above ~1 T. At high fields, the sample exhibited clear SdH oscillations, which disappeared quickly once the sampled was tilted away from perpendicular configuration. In the parallel field configuration, the MR is negligible, similar to the sample #1. Note that for this experiment the sample was rotated in such a way that the in-plane magnetic field was parallel to the current at $\theta = 90°$ (Figure 3c inset), in contrast to the rotation scheme for sample #1. However, the magneto-transport effects are qualitatively the same. This leads us to believe that the surface state on the side walls of Bi_2Se_3 nanoribbons has low mobility and does not contribute much to the observed MR.

To analyze the SdH oscillations, we subtract the linear MR background from the raw $R(B)$ data in Figure 3a, and the residual oscillatory part of the MR is shown in Figure 3b for $\theta = 0°$, 10°, 22°, 35° (from top to bottom curve). As can be seen, when the sample was tilted, the SdH oscillations move to higher field, and eventually our magnetic field (9 T) is not large enough to track the SdH oscillations at $\theta > 35°$. By comparing the magnetic field values at the SdH dips we could assign the Landau level filling factor ν to be 7 and 8 for the two dips observed at 7.7 and 6.9 T at $\theta = 0$. In Figure 3c, we plot the positions of $\nu = 7$ and 8 against the tilt angle θ, as the sample is tilted away from the perpendicular orientation. The four data points for $\nu = 8$ dip are seen to follow the $1/\cos(\theta)$ function nicely. For $\nu = 7$, the dip was observable only at $\theta = 0°$, 10°, and 22° and moved outside our field range (9 T). However, we infer its position at $\theta = 35°$ by multiplying the $\nu = 8$ dip position with 8/7. This inferred value together with the three points at lower tilt angle also obeys the $1/\cos(\theta)$ dependence. The agreement between the $1/\cos(\theta)$ function (black lines) and our angle-dependent SdH position suggests that the observed SdH oscillations are likely to originate from a 2D Fermi surface.

Plotting the Landau index ν of the SdH peak and dip positions *vs* the inverse of the magnetic field, $1/B$, we obtain a linear dependence in Figure 3d. The slope of the ν *vs* $1/B$ plot gives a 2D sheet carrier density of $1.3 \times 10^{12}/cm^2$. This carrier density corresponds to a Fermi momentum $k_F = 0.41$ nm^{-1} and Fermi energy $E_F = \nu_F \hbar k_F = 110$ meV. On the basis of ARPES results,[6,13] the bottom of the conduction band is 205 meV above the Dirac point in Bi_2Se_3. We thus estimate that the position of the 2D surface-state Fermi energy is ~95 meV below the bottom of the bulk conduction band, consistent with the fact that 3D magneto-transport is negligible in our samples. While both 2D electrons in conventional semiconductors and 2D Dirac electrons have linear ν *vs* $1/B$ dependence, the different Berry's phase would make the intercept zero for regular 2D electrons and nonzero for Dirac electrons with nonzero Berry's phase.[24] The linear fit of $\nu(1/B)$ in Figure 3d produces an intercept of -0.2 ± 0.2. The relatively large uncertainty is due to the limited number of SdH oscillations observed, making it ambiguous to infer the existence of Berry's phase from a simple analysis of $\nu(1/B)$. In such a case, it is more useful to directly compare the magneto-resistance data with the known SdH oscillation of 2D electrons, and a nonzero Berry's phase would manifest as a phase shift in the oscillations.[25] The general expression for SdH oscillation is[26]

$$\Delta R(B) = A \exp(-\pi/\mu B)\cos[2\pi(B_F/B + 1/2 + \beta)] \quad (1)$$

In eq 1, B_F is the frequency of SdH oscillation in $1/B$, and $\beta \times 2\pi$ is the Berry's phase. The amplitude A has the following temperature dependence:

$$A \propto \frac{2\pi^2 k_B T/\hbar\omega_c}{\sinh(2\pi^2 k_B T/\hbar\omega_c)} \quad (2)$$

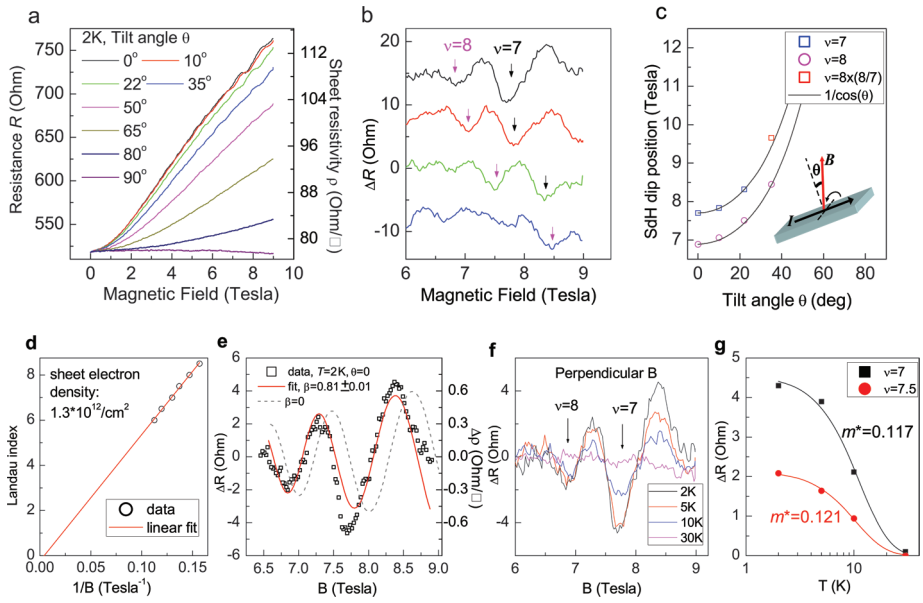

Figure 3. 2D Shubnikov−de Haas (SdH) oscillations in a Bi_2Se_3 nanoribbon. (a) MR of sample #2 between 0 and 9 T at $T = 2$ K when the rotation angle θ is increased from 0° to 90° (the rotation scheme is shown as an inset in panel c). SdH oscillations are visible on top of the linear MR background for the perpendicular field ($\theta = 0°$) and disappear rapidly as θ increases. (b) SdH oscillations at $\theta = 0° \rightarrow 35°$ after subtracting background MR. The black and pink arrows mark the SdH dips at a Landau filling factor $\nu = 7$ and 8. (c) Position of the $\nu = 7$ or 8 SdH dip plotted against rotation angle. The data are consistent with the $1/\cos(\theta)$ dependence (gray lines), which is expected for 2D SdH oscillations. The inset shows the rotation configuration. (d) Landau index ν plotted against the inverse of the magnetic field for the SdH oscillations in perpendicular field ($\theta = 0°$). The slope of linear fit gives a sheet electron density of $n \approx 1.3 \times 10^{12}/cm^2$. (e) Fitting of the SdH oscillation at 2 K and $\theta = 0$. A nonzero Berry's phase ($\beta = 0.81$) is obtained to match the phase of SdH oscillations. (f) SdH oscillations at different T. (g) Fitting the amplitudes of the SdH dip/peak at $\nu = 7$ and 7.5 *vs* T yields an effective electron mass $m^* = 0.117$ and $0.121 \pm 0.007 \times m_e$.

Using the B_F extracted from the slope of the $\nu(1/B)$ dependence, we fit the residual SdH oscillations in $R(B)$ at $T = 2$ K to eq 1 with three fitting parameters: A, β, and μ. The fitting yielded a nonzero Berry's phase $\beta = 0.81 \pm 0.01$ together with $A = 90 \pm 50$ Ohm and $\mu = 0.12 \pm 0.02$ $m^2/(V\ s)$, as shown by the solid red line in Figure 3e. On the other hand, $\beta = 0$ with the same A and μ would predict an oscillatory pattern (dashed gray line in Figure 3e) clearly shifted from experimental data. For 2D Dirac electrons, the Berry's phase of π should lead to $\beta = 0.5$. However, extracting Berry's phase from SdH of the surface state in Bi compound topological insulators is complicated, as the application of a magnetic field itself may have an influence on the value of β.[18,27] Therefore, a more systematic study on samples with higher mobility in higher magnetic fields (so there are more SdH oscillations) is needed to clarify the Berry's phase effect in Bi_2Se_3 nanoribbons. Note that our fitted mobility $\mu = 0.12$ $m^2/(V\ s)$ should be an underestimate since the mobility μ in eq 1 is defined with the quantum lifetime τ_q, which is normally shorter than the transport scattering time τ in the standard definition of mobility ($\mu = e\tau/m^*$) due to the dominance of small angle scattering contribution in τ.

Figure 3f shows the temperature effect on SdH oscillations. As expected, SdH oscillation amplitude decreases at higher temperature due to the thermal smearing of Landau levels. Fitting the temperature dependence of SdH amplitude to eq 2 allows us to extract m^*, the effective mass of 2D electrons in our Bi_2Se_3 nanoribbon. The experimental amplitudes of the SdH peak/dip at $\nu = 7$ and 7.5 *vs* temperature are shown in Figure 3g together with fitting curves. Both fitting results yield $m^* \approx 0.12m_e$, with m_e being the free electron mass. This value is in quantitative agreement with recent magneto-transport experiment on surface state in bulk Bi_2Se_3 crystals with reduced electron densities.[27]

Now let us turn back to the main finding of the paper: the linear magneto-resistance induced by 2D magneto-transport. Due to the 2D nature of this linear MR and the associated SdH oscillations, it is likely that this linear MR is intrinsically tied to the 2D Dirac electrons occupying the surface state. It would be curious if such surface-state magneto-transport can be exploited at high temperature (*e.g.*, room temperature) relevant for device applications. We found that raising temperature to room temperature does not have a significant influence on the linear MR as shown in Figure 4. In Figure 4a, where the MR of sample #2 is plotted at various T from 2 to 300 K, one sees that the linear MR at $B_\perp > 1$ T remains unchanged. At the same time, the parallel magnetic field induces negligible MR, as shown by the data at $T = 2$, 150, and 300 K. The angular dependence of MR suggests that the MR is a 2D response over the whole temperature range from 2 to 300 K, as illustrated by the good agreement between experimental resistance *vs* tilt angle data at 9 T and the $|\cos(\theta)|$ function in Figure 4b.

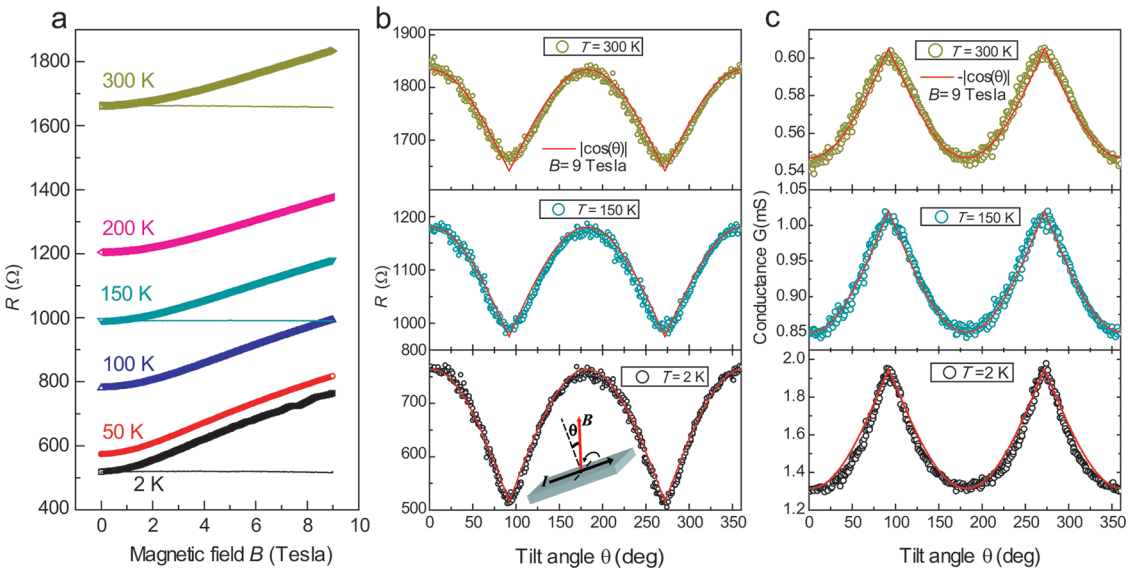

Figure 4. 2D linear magneto-resistance persisting to room temperature. (a) Resistance *vs* magnetic field of sample #2 from T = 2 to 300 K. The data in the perpendicular field are shown as dots, while the data in the parallel field are shown as solid lines for T = 2, 150, and 300 K. (b) R *vs* rotation angle at T = 2, 150, and 300 K. The function $|\cos(\theta)|$ is shown as solid red lines. (c) Conductance of Bi_2Se_3 nanoribbon sample #2 *vs* rotation angle at T = 2, 150, and 300 K. Red solid lines represent the function $-|\cos(\theta)|$, which is seen to describe the conductance data well for all temperatures.

Since both the bulk conduction and surface conduction contribute to the total conductance in Bi_2Se_3 crystals, it is more appropriate to discuss conductance G instead of resistance in a quantitative analysis. In Figure 4c, we show G *vs* θ at 2, 150, and 300 K by inverting resistance data in Figure 4b. It can be seen that the function $-|\cos(\theta)|$ also matches $G(\theta)$ very well. Therefore, the magneto-transport effect we report has a 2D nature and is robust from 2 K to room temperature in the magneto-conductance picture. However, due to the increased resistance at high temperatures from phonon scattering, the magneto-conductance at 300 K is nearly 10 times smaller than at 2 K. This is reasonable given that the thermal energy scale at 300 K already exceeds the maximal cyclotron energy $\hbar\omega_c$ (~100 K) at 9 T, the highest magnetic field in our experiment. If we model the total resistance as $R = 1/(G_b + G_s)$ with G_b and G_s as the bulk and surface conductance, a smaller magneto-conductance $\Delta G_s(B)$ for the surface state at high temperature is compensated by the smaller value of G_b and still converts into a relatively constant $\Delta R(B)$ in the measurement of total resistance at different T. Yet due to the striking robustness of linear MR against increasing temperature and the importance of MR in magneto-electronic device applications, here we emphasize the MR instead of magneto-conductance in this paper. We suggest that this linear MR could be exploited in magneto-electronic device operation over a wide temperature range, and its magnitude is likely to become larger once the nanoribbon crystal quality and mobility improve.[18]

We would like to conclude with a discussion about the possible origins of the linear MR and its relation with other findings in materials with a Dirac electronic dispersion spectrum. The well-established Kohler's rule[21] suggests that the MR of a material is a universal function of μB: $R(B)/R(0) = F(\mu B)$. It is common[21] that at low field when $\mu B < 1$, $F(\mu B) \approx 1 + (\mu B)^2$, as a result of the Lorentz force deflection of carriers. At high field condition μB, or $\omega_c\tau > 1$, most materials show saturating MR, and a nonsaturating and linear MR is unusual. For metals with open Fermi surfaces (*e.g.*, Au), the MR could be linear and nonsaturating at high fields.[21] This is not the case here for Bi_2Se_3. The existence of a linear MR for a small band gap semiconductor could have a quantum[20,28,29] or classical origin.[19,22] To explain the linear MR down to very low fields in silver chalcogenides,[19] Abrikosov first proposed a model based on the quantum-MR[28,29] for systems with a gapless linear dispersion spectrum.[28] It is believed that such gapless linear dispersion may apply for silver chalcogenides or other small band gap semiconductors with a strong inhomogeneity.[20,28] Abrikosov's linear quantum-MR was originally developed at the extreme quantum limit $\hbar\omega_c > E_F$, when all electrons coalesce into the lowest Landau level. Another requirement is that $\omega_c\tau$ or $\mu B > 1$, *i.e.*, that Landau levels are well-formed. From the above discussions and SdH data, we see that indeed the linear MR occurs at high magnetic field regime where $\mu B > 1$ (note that our estimate of $\mu \approx 0.12\ m^2/(V\ s)$ is an underestimate) and SdH oscillations start to appear. However, there is clearly more than one Landau level occupied in our sample in the field range where linear MR was observed. This does not exclude the linear quantum-MR as the explanation for our data though, since previous experimental study on polycrystal InSb showed that the linear quantum-MR could appear at much lower field with more than

one Landau level filled.[20] Graphite and epitaxial graphene are also known to exhibit linear MR.[30−33] The linear MR in epitaxial graphene was found to persist to room temperature and was interpreted as due to Abrikosov's linear quantum-MR.[33] However, in order to fully reconcile our experimental data with the linear quantum-MR, further theoretical study is required to understand the fate of linear quantum-MR at high temperatures where $k_BT > \hbar\omega_c$.

Without invoking the linear dispersion spectrum, Parish and Littlewood suggested a classical origin for linear MR in which the MR is a consequence of mobility fluctuations in a strongly inhomogeneous system.[22] For our Bi_2Se_3 nanoribbons, the single-crystal quality and small length scale of the device rule out the strong physical inhomogeneity of the sample surface (AFM imaging also showed only a few quintuple-layer step edges over the 1 μm length of the nanoribbon). However, we cannot exclude the possibility of strong electronic inhomogeneity being responsible for the linear MR in our Bi_2Se_3 nanoribbon. Electron and hole puddles and charge inhomogeneity have been observed in high-quality graphene samples *via* local probe techniques.[34,35] It is quite reasonable that such spatial inhomogeneity of carriers can also exist for a gapless surface state on topological insulators.

CONCLUSION

In summary, we report a linear MR induced by 2D magneto-transport in chemically synthesized nanoribbons of topological insulator Bi_2Se_3. When the magnetic field is parallel to the surface of a nanoribbon ($a-b$ plane), the MR effect is negligible compared to the MR in perpendicular magnetic fields. The angular dependence of the MR showed an exact $|\cos(\theta)|$ dependence at arbitrary angle, illustrating the 2D origin of linear MR. Angle-dependent SdH oscillations also suggest the existence of a 2D Fermi surface. These results suggest that the linear MR is likely related to 2D surface-state conduction.[36] Furthermore, it is striking that this 2D magneto-transport-induced linear MR persists at room temperature, underscoring the potential of exploiting 2D topological surface states for magneto-electronic device applications over a broad temperature range.

METHODS

Bi_2Se_3 Nanowire and Nanoribbon Synthesis and Characterization. Pure Bi_2Se_3 nanowires and nanoribbons are synthesized in a single zone horizontal tube furnace (Lindberg/Blue M) *via* the vapor−liquid−solid mechanism with gold nanoparticles as catalysts, similar to the literature procedure.[10,11] Bi_2Se_3 powder is placed and evaporated at the center of a one-inch-diameter quartz tube fitted inside the tube furnace to provide the Bi/Se vapor. Silicon (100) substrate functionalized with 10 nm gold nanoparticles (Sigma Aldrich) is placed downstream of the Bi/Se vapor flow and used as the wafer supporting the nanowire or nanoribbon growth. Prior to nanoparticle functionalization, the silicon substrate was functionalized with 0.1% w/v aqueous poly-L-lysine solution (Ted Pella) to promote the linking of gold nanoparticles to the substrate surface. Before nanoribbon growth, the system is pumped to a base pressure of 5 mTorr (limited by the mechanical pump) and flushed with Ar/H_2 (10%) gas. Bi_2Se_3 powder (99.999% from Alfa Aesar) is evaporated at 680 °C under the pressure of 200 Torr in 100 sccm flow of Ar/H_2 (10%). Typical growth time is 1.5 to 2 h. After the system cools, the silicon substrate is covered with a gray coating layer, which consists of Bi_2Se_3 nanowires and nanoribbons.

The field-emission SEM Hitachi S4500 gun is used to characterize the morphology of synthesized Bi_2Se_3 nanoribbons. The crystal structure and chemical composition of the Bi_2Se_3 nanoribbons are characterized by a TECNAI F30 300 kV field-emission gun energy-filtering high-resolution scanning transmission electron microscope (HRTEM) and energy-dispersive X-ray spectroscopy equipped in the TEM.

Acknowledgment. X.P.A.G. acknowledges P. B. Littlewood, Y. Cui, and Y. P. Chen for discussions, ACS Petroleum Research Fund (grant 48800-DNI10), and NSF (grant DMR-0906415) for financial support.

REFERENCES AND NOTES

1. Zhang, S. C. Topological States of Quantum Matter. *Physics* **2008**, *1*, 6.
2. Moore, J. E. The Birth of Topological Insulators. *Nature* **2010**, *464*, 194–198.
3. Hasan, M. Z.; Kane, C. L. Topological Insulators. *Rev. Mod. Phys.* **2010**, *82*, 3045–3067.
4. Qi, X. L.; Zhang, S. C. Topological Insulators and Superconductors. *arXiv*: 1008.2026. [online] http://xxx.lanl.gov/PS_cache/arxiv/pdf/1008/1008.2026v1.pdf (accessed July 29, 2011).
5. Zhang, H. J.; Liu, C. X.; Qi, X. L.; Dai, X; Fang, Z; Zhang, S. C. Topological Insulators in Bi_2Se_3, Bi_2Te_3 and Sb_2Te_3 with a Single Dirac Cone on the Surface. *Nat. Phys.* **2009**, *5*, 438–442.
6. Xia, Y.; Qian, D.; Hsieh, D.; Wray, L.; Pal, A.; Lin, H.; Bansil, A.; Grauer, D.; Hor, Y. S.; Cava, R. J.; *et al.* Observation of a Large-Gap Topological Insulator Class with a Single Dirac Cone on the Surface. *Nat. Phys.* **2009**, *5*, 398–402.
7. Hsieh, D.; Xia, Y.; Qian, D.; Wray, L.; Dil, J. H.; Meier, F.; Osterwalder, J.; Patthey, L.; Checkelsky, J. G.; Ong, N. P.; *et al.* A Tunable Topological Insulator in the Spin Helical Dirac Transport Regime. *Nature* **2009**, *460*, 1101–1105.
8. Chen, Y. L.; Analytis, J. G.; Chu, J. H.; Liu, Z. K.; Mo, S. K.; Qi, X. L.; Zhang, H. J.; Lu, D. H.; Dai, X.; Fang, Z.; *et al.* Experimental Realization of a Three-Dimensional Topological Insulator, Bi_2Te_3. *Science* **2009**, *325*, 178–181.
9. Hsieh, D.; Qian, D.; Wray, L; Xia, Y.; Hor, Y. S.; Cava, R. J.; Hasan, M. Z. A Topological Dirac Insulator in a Quantum Spin Hall Phase. *Nature* **2008**, *452*, 970–974.
10. Peng, H.; Lai, K.; Kong, D.; Meister, S.; Chen, Y. L.; Qi, X. L.; Zhang, S. C.; Shen, Z. X.; Cui, Y. Aharonov-Bohm Interference in Topological Insulator Nanoribbons. *Nat. Mater.* **2010**, *9*, 225–229.
11. Kong, D.; Randel, J. C.; Peng, H.; Cha, J. J.; Meister, S.; Lai, K.; Chen, Y. L.; Shen, Z. X.; Manoharan, H. C.; Cui, Y. Topological Insulator Nanowires and Naonribbons. *Nano Lett.* **2010**, *10*, 329–333.
12. Checkelsky, J. G.; Hor, Y. S.; Liu, M. H.; Qu, D. X.; Cava, R. J.; Ong, N. P. Quantum Interference in Macroscopic Crystals of Nonmetallic Bi_2Se_3. *Phys. Rev. Lett.* **2009**, *103*, 246601.
13. Analytis, J. G.; Chu, J. H.; Chen, Y. L.; Corredor, F.; McDonald, R. D.; Shen, Z. X.; Fisher, I. R. Bulk Fermi Surface Coexistence with Dirac Surface State in Bi_2Se_3:a Comparison of Photoemission and Shubnikov-De Haas Measurements. *Phys. Rev. B* **2009**, *81*, 205407.

14. Eto, K.; Ren, Z.; Taskin, A. A.; Segawa, K.; Ando, Y. Angular-Dependent Oscillations of the Magnetoresistance in Bi_2Se_3 Due to the Three-Dimensional Bulk Fermi Surface. *Phys. Rev. B* **2010**, *81*, 195309.
15. Butch, N. P.; Kirshenbaum, K.; Syers, P.; Sushkov, A. B.; Jenkins, G. S.; Drew, H. D.; Paglione, J. Strong Surface Scattering in Ultrahigh Mobility Bi_2Se_3 Topological Insulator Crystals. *Phys. Rev. B* **2010**, *81*, 241301.
16. Steinberg, H.; Gardner, D. R.; Lee, Y. S.; Jarillo-Herrero, P. Surface State Transport and Ambipolar Electric Field Effect in Bi_2Se_3 Nanodevices. *Nano Lett.* **2010**, *10*, 5032–5036.
17. Checkelsky, J. G.; Hor, Y. S.; Cava, R. J.; Ong, N. P. Surface State Conduction Observed in Voltage-Tuned Crystals of the Topological Insulator Bi_2Se_3. *Phys. Rev. Lett.* **2011**, *106*, 196801.
18. Qu, D. X.; Hor, Y. S.; Xiong, J.; Cava, R. J.; Ong, N. P. Quantum Oscillations and Hall Anomaly of Surface States in the Topological Insulator Bi_2Te_3. *Science* **2010**, *329*, 821–824.
19. Xu, R.; Husmann, A.; Rosenbaum, T. F.; Saboungi, M. L.; Enderby, J. E.; Littlewood, P. B. Large Magnetoresistance in Non-Magnetic Silver Chalcogenides. *Nature* **1997**, *390*, 57–60.
20. Hu, J. S.; Rosenbaum, T. F. Classical and Quantum Routes to Linear Magnetoresistance. *Nat. Mater.* **2008**, *7*, 697–700.
21. Olsen, J. L. *Electron Transport in Metals*; Interscience: New York, 1962.
22. Parish, M. M.; Littlewood, P. B. Non-saturating Magnetoresistance in Heavily Disordered Semiconductors. *Nature* **2003**, *426*, 162–165.
23. Fan, Z.; Ho, J. C.; Jacobson, Z. A.; Yerushalmi, R.; Alley, R. L.; Razavi, H.; Javey, A. Wafer-Scale Assembly of Highly Ordered Semiconductor Nanowire Arrays by Contact Printing. *Nano Lett.* **2008**, *8*, 20–25.
24. Zhang, Y. B.; Tan, Y. W.; Stormer, H. L.; Kim, P. Experimental Observation of the Quantum Hall Effect and Berry's Phase in Graphene. *Nature* **2005**, *438*, 201–204.
25. Luk'yanchuk, I. A.; Kopelevich, Y. Phase Analysis of Quantum Oscillations in Graphite. *Phys. Rev. Lett.* **2004**, *93*, 166402.
26. Isihara, A.; Smrcka, L. Density and Magnetic Field Dependences of the Conductivity of Two-Dimensional Electron Systems. *J. Phys. C: Solid State Phys.* **1986**, *19*, 6777–6789.
27. Analytis, J. G.; McDonald, R. D.; Riggs, S. C.; Chu, J. H.; Boebinger, G. S.; Fisher, I. R. Two-Dimensional Dirac Fermions in a Topological Insulator: Transport in the Quantum Limit. *Nat. Phys.* **2010**, *6*, 960–964.
28. Abrikosov, A. A. Quantum Magnetoresistance. *Phys. Rev. B* **1998**, *58*, 2788–2794.
29. Abrikosov, A. A. Quantum Linear Magnetoresistance. *Europhys. Lett.* **2000**, *49*, 789.
30. McClure, J. W.; Spry, W. J. Linear Magnetoresistance in the Quantum Limit in Graphite. *Phys. Rev.* **1968**, *165*, 809.
31. Zhang, Y.; Small, J. P.; Amori, M. E.S.; Kim, P. Electric Field Modulation of Galvanomagnetic Properties of Mesoscopic Graphite. *Phys. Rev. Lett.* **2005**, *94*, 176803.
32. Morozov, S. V.; Novoselov, K. S.; Schedin, F.; Jiang, D.; Firsov, A. A.; Geim, A. K. Two-Dimensional Electron and Hole Gases at the Surface of Graphite. *Phys. Rev. B* **2005**, *72*, 201401.
33. Friedman, A. L.; Tedesco, J. L.; Campbell, P. M.; Culbertson, J. C.; Aifer, E.; Perkins, F. K.; Myers-Ward, R. L.; Hite, J. K.; Eddy, C. R.; Jernigan, G. G.; *et al.* Quantum Linear Magnetoresistance in Multilayer Epitaxial Graphene. *Nano Lett.* **2010**, *10*, 3962–3965.
34. Martin, J.; Akerman, N.; Ulbricht, G.; Lohmann, T.; Smet, J. H.; Klitzing, K. V.; Yacoby, A. Observation of Electron-Hole Puddles in Graphene Using a Scanning Single-Electron Transistor. *Nat. Phys.* **2008**, *4*, 144–148.
35. Zhang, Y.; Brar, V. W.; Girit, C.; Zettl, A.; Crommie, M. F. Origin of Spatial Charge Inhomogeneity in Graphene. *Nat. Phys.* **2009**, *5*, 722–726.
36. Some recent angle-dependent SdH and Hall experiments on exfoliated Bi_2Se_3 flakes raised the question whether such 2D magneto-transport may be related to the conduction within each individual quintuple layer. (Y. P. Chen, private communication and APS March meeting abstract P35.00012). Such a possibility remains to be understood, and it is unclear if it is related to our data here.